Exciton states and optical transitions in colloidal CdS quantum dots: Shape and dielectric mismatch effects

V. A. Fonoberov* and E. P. Pokatilov[†]

Laboratory of Multilayer Structure Physics, Department of Theoretical Physics, State University of Moldova, A. Mateevici 60, MD-2009 Chişinău, Moldova

A. A. Balandin

Department of Electrical Engineering, University of California at Riverside, Riverside, California 92521

We present a theoretical investigation of electron-hole and exciton energy spectra as well as oscillator strengths of optical transitions in colloidal CdS quantum dots (QD's) with spherical and tetrahedral shape. The Coulomb potential energy of the electron-hole system is treated taking into account the dielectric mismatch at the QD boundaries. Calculation of electron-hole energy spectrum and Coulomb potential energy in tetrahedral QD's is carried out using the finite difference method. It is shown that the bulk Coulomb potential energy with the dielectric constant of QD leads to lower exciton energy levels as compared to the Coulomb potential, which includes electron-hole interaction and self-action energies. The Coulomb potential changes the electron-hole pair energies without dielectric confinement contributions in such a way that the exciton ground state becomes active for optical transitions in dipole approximation for both tetrahedral and spherical QD's while the lowest electron-hole pair energy level is active for tetrahedral and passive for spherical QD's. The exciton binding energy in both types of QD's is enhanced by a factor of 2 in the presence of the dielectric mismatch. It is proven that the inclusion of the real QD shape and dielectric mismatch is important not only for the quantitative analysis but also for the qualitative description of optical properties of colloidal CdS QD's.

I. INTRODUCTION

One of the most important features of low-dimensional semiconductor structures is the confinement driven quantization of energy spectrum of charge carriers. The effect of quantum confinement becomes stronger as the confinement dimension increases and the size of a structure decreases. While bulk materials have a three-dimensional energy band structure, one-dimensional confinement of quantum wells leads to a two-dimensional energy band structure near each quantized energy level in the well and two-dimensional confinement of quantum wires leads to a one-dimensional energy band structure near each quantized energy level in the wire. At the same time, three-dimensional confinement in quantum dots (QD's) leads to a discrete (atomiclike) lower part of the energy spectrum. When the effective dimensions of a QD are less than the bulk exciton Bohr radius, the exciton energy spectrum is primarily defined by the confinement, while the Coulomb interaction plays a minor role.

In order to predict novel physical phenomena and suggest new technical applications, researchers investigate manifestations of quantum-size effects in nanostructures both theoretically and experimentally.[1,2] Not long ago, extremely high-quality superlattices, multilayers, and monolayer semiconductor structures have been fabricated.[3] Energy spectra of charge carriers and excitons in quantum wires with rectangular, T-shaped, V-groove, and other cross sections have been investigated.[4–10] Recently, a significant attention has been attracted to QD's due to their promise for applications as basic elements for semiconductor lasers, nonlinear transformers of light, computer memory, and elements of quantum logic gates.[11–13]

Some of the most effective methods of investigation of carrier energy spectra in QD's are optical ones. They include absorption of light, photoluminescence, photoluminescence excitation, Raman scattering, etc.[14–19] At the same time, the present-day technology does not allow the synthesis of arrays of QD's with identical shape, size, and orientation. Therefore, experimentally obtained characteristics of QD's are averaged and include statistical properties of the ensemble. It should be mentioned, however, that there are special methods that allow for observation of optical characteristics of single QD's.[20–22] The crystal structure and shape of QD's depends mainly on the growth conditions. For instance, colloidal CdSe QD's with hexagonal crystallinity, as well as CdSe, CdS_xSe_{1-x}, PbS, and PbSe QD's grown in glasses, have nearly spherical shape.[15,16,23–25] Electrochemically self-assembled CdS QD's in the Al_2O_3 matrix have quasicylindrical shape.[26,27] InAs/GaAs QDs are pyramidal with square base,[28,29] and GaN/AlN QD's are truncated hexagonal pyramids.[30] Alkali-haloid nanocrystals in an alkali-haloid matrix usually form rectangular prisms.[31]

The key problem in the investigation of optical properties of QD's is finding the energy spectrum of confined charge carriers and the corresponding wave functions. The Coulomb interaction of an electron and a hole in the exciton influences the energy of optical absorption and photoluminescence and splits the degenerate electron-hole pair levels. In parabolic, one-band, and infinite barrier approximations for structures with simple geometrical shapes (planar, cylindrical, spherical), the energy spectrum can be found from general expression $E_n \sim \alpha_n^2/R^2$, where $\alpha_n(n=1,2,\dots)$ are numbers close to a corresponding real number n, R is a characteristic di-

mension of the system, e.g., thickness of the layer, radius of the cylinder, or radius of the sphere. Nonparabolicity of energy bands, degeneracy of valence bands, and finiteness of potential barriers strongly complicate the structure of the size-quantized energy spectrum. In this case, the detailed solution of the Schrödinger equation is needed even for spherical QD's. Nevertheless, a spherically symmetric QD, having the simplest shape, is commonly used in the so-called spherical approximation for description of electronic and optical properties of QD's. In particular, CdS/HgS/CdS quantum-dot quantum wells (QDQW's), grown[32,33] in an aqueous solution, are considered[34−36] spherical. There are several stages in the QDQW growth. First, the core of the future structure—a CdS tetrahedron with cubic crystal lattice is formed. After subsequent growing of the HgS and CdS monolayers onto the surface of the core, the shape of the nanocrystal becomes a truncated tetrahedron, what is, indeed, closer to spherical shape than to tetrahedral one. Therefore, for simplicity, in all previous theoretical calculations aimed to interpret the optical properties of QDQW's, the shape of the nanocrystal was considered spherical.

The dielectric mismatch at the interfaces of low-dimensional structures is also known to have a considerable effect on the exciton energies. The dielectric enhancement of excitons has been demonstrated in quantum wells[37] and in quantum wires.[38] A similar effect is expected in QD's.[39]

Not only multiple QDQW's, but also single CdS QD's have been studied experimentally.[21,22] Thus, it is important to investigate electron, hole, and exciton spectra as well as optical properties of colloidal CdS nanocrystals taking into account both shape (tetrahedral or spherical[40]) and dielectric mismatch effects. The comparison of the theoretical results with experiment will help in interpretation of the experimental data. Since experimental data is available for CdS QD's with diameters from one to ten nanometers it is also interesting to compare the validity of different theoretical methods for description of exciton spectra in a range of QD sizes.

II. THEORY

A. Electron and hole states

We consider colloidal CdS QD's with cubic crystal lattice. Since the band gap of bulk CdS is wide (2.5 eV), we study electron and hole states of spherical and tetrahedral QD's by using separate one-band electron and six-band hole effective-mass Hamiltonians. The band gap of the exterior medium—H_2O is about 8 eV, therefore potential barriers for both electrons and holes in CdS QD's with diameters larger than 2 nm are so high that they can safely be considered infinite. Thus, the infinite barrier approximation is used in this paper.

In the presence of the dielectric mismatch, the electron (hole) energy ($E_{e(h)}$) can be separated into a quantum confinement energy ($E_{e(h)}^{QC}$), which describes the electron (hole) confinement energy in the absence of the dielectric mismatch, and dielectric confinement contribution ($\Delta E_{e(h)}^{DC}$), which describes the self-action energy of an electron (hole) in the electrostatic potential generated by its own image charge due to the dielectric constant discontinuity at the QD boundary. Further in Sec. II A, we consider only quantum

confinement electron and hole states in QD's. The index QC will be omitted. To calculate the exciton states, the dielectric confinement contribution to the electron and hole energies will be taken into account in Secs. II B and II C as a part of the Coulomb potential energy of the electron-hole system.

1. Spherical QD

The one-band effective-mass Schrödinger equation for the envelope wave function of an electron in a QD has the form

$$-\frac{\hbar^2}{2m_e}\nabla^2\Phi_e(\mathbf{r})+U_e(\mathbf{r})\Phi_e(\mathbf{r})=E_e\Phi_e(\mathbf{r}), \quad (1)$$

where m_e is the electron effective mass and $U_e(\mathbf{r})$ is the electron confinement potential energy, which is equal to zero inside the QD and infinity outside the QD; E_e and $\Phi_e(\mathbf{r})$ are the quantum confinement electron eigenenergy and the corresponding envelope wave function. The solution of Eq. (1) for a spherical QD with radius R is well known and can be written as

$$\Phi_e^{l,m,n}(\mathbf{r})=A_{l,n}j_l\left(\alpha_{l,n}\frac{r}{R}\right)Y_{l,m}(\theta,\phi), \quad (2)$$

where $A_{l,n}$ is a normalization coefficient, $j_l(x)$ is a spherical Bessel function, $\alpha_{l,n}$ is the nth zero of the function $j_l(x)$, and $Y_{l,m}(\theta,\phi)$ is the spherical harmonic. In Eq. (2), n is radial and l,m are angular quantum numbers. Due to the spherical symmetry, the eigenenergy

$$E_e^{l,n}=\frac{\hbar^2}{2m_e}\left(\frac{\alpha_{l,n}}{R}\right)^2 \quad (3)$$

is $(2l+1)$-fold degenerate with respect to the angular momentum projection m. Common notations nS, nP, nD, $\ldots$, are used to describe eigenstates (3) with angular momenta $l=0,1,2,\ldots$, respectively.

The six-band Hamiltonian for a hole in a spherical QD is given in Ref. 40 in the spherical approximation. The solution of the corresponding Schrödinger equation can be written in the following analytical form:

$$\Psi_h^{j,m,p,n}(\mathbf{r})=\sum_{J=1/2}^{3/2}\sum_{\mu=-J}^{J}\Phi_{J,\mu}^{j,m,p,n}(\mathbf{r})i^{(J-\mu)(2-2J)}u_{J,\mu}, \quad (4)$$

where $u_{J,\mu}$ are the Bloch functions of the valence band[41] and $\Phi_{J,\mu}^{j,m,p,n}(\mathbf{r})$ are the envelope functions given by

$$\Phi_{J,\mu}^{j,m,p,n}(\mathbf{r})=\sum_{l=|j-J|}^{j+J}{}'\sum_{\lambda=-l}^{l}C_{J,\mu;l,\lambda}^{j,m}R_{J,l}^{j,p,n}(r)Y_{l,\lambda}(\theta,\phi). \quad (5)$$

Here, $C_{J,\mu;l,\lambda}^{j,m}$ are the Clebsch-Gordan coefficients and $R_{J,l}^{j,p,n}(r)$ are the radial envelope functions, which can be found as a linear combination of few functions $j_l(x)$ or $i_l(x)$ [$i_l(x)$ is a spherical Bessel function of the second kind]. The prime near the first sum in Eq. (5) shows that only values of l satisfying equality $(-1)^{j-l+1/2}\equiv p$ should be taken, where $p=\pm 1$ is the conserved parity. Another quantum numbers in
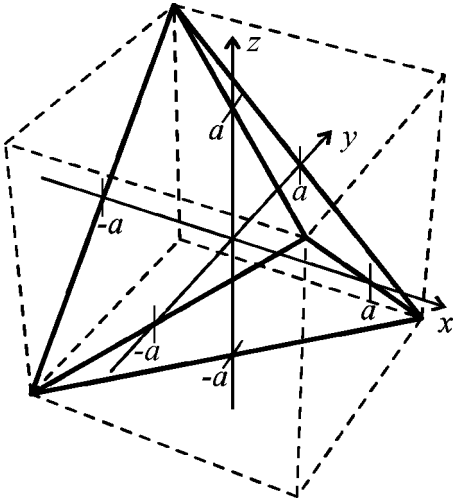
FIG. 1. Orientation and dimensions of a tetrahedral QD. a is the distance from the center of the tetrahedron to the middle of its edge.

Eq. (4) are j,m (angular) and n (radial). The eigenenergy $E_h^{j,p,n}$, which can be found applying the boundary condition $\Psi_h^{j,m,p,n}(\mathbf{r})|_{r=R}=0$ to the wave function (4), is $(2j+1)$-fold degenerate with respect to the projection m of the total angular momentum j. Common notations nQ_j are used to describe hole eigenstates, where symbol $Q=S,P,D,\ldots,$ corresponds to the lowest value of momentum l in Eq. (5), i.e., $\min(j+p/2,|j-3p/2|)$.

2. Tetrahedral QD

To obtain electron states in the tetrahedral QD, the Schrödinger equation (1) is numerically solved using a finite difference method. Let us choose the coordinate system for the considered tetrahedral QD as shown in Fig. 1. A uniform grid with step length $2a/N$ is introduced in the cube with edge $2a$ (dashed cube in Fig. 1) circumscribed about the tetrahedron. The grid has $(N-1)^3$ nodes inside the cube, which is split into N^3 cubic cells. To satisfy the hard wall boundary conditions, wave functions are set to zero at the surface and outside the tetrahedron. Therefore, it is necessary to consider only $\mathcal{N}=(N-1)[(N-1)^2+2]/3$ nodes inside the tetrahedron. The eigenvalues and eigenvectors of the resulting $\mathcal{N}\times\mathcal{N}$ Hamiltonian matrix are computed using a modified Davidson-Liu algorithm.[42] The calculation does not take advantage of the tetrahedral symmetry of the problem. It is known from the group theory, that the degeneracy λ of electron eigenenergies in a tetrahedral QD can be onefold, twofold, or threefold. As seen from Eq. (1), the dependence of the energy levels on the QD dimension a has a form similar to Eq. (3)

$$E_a^{\lambda,\nu}=\left(\frac{a_0}{a}\right)^2 E_{a_0}^{\lambda,\nu} \qquad (6)$$

and, as a consequence of the normalization, corresponding envelope wave functions depend on a as

$$\Phi_a^{\lambda,\mu,\nu}(\mathbf{r})=\left(\frac{a_0}{a}\right)^{3/2}\Phi_{a_0}^{\lambda,\mu,\nu}\left(\frac{a_0}{a}\mathbf{r}\right), \qquad (7)$$

where ν is the number of the level with degeneracy λ, $\mu=1,\ldots,\lambda$ counts degenerate states, and $a_0=$const. Using Eqs. (6) and (7) one can find the eigenstates for a tetrahedral QD with arbitrary size knowing the solution of Eq. (1) for $a=a_0$.

The six-band Hamiltonian for a hole in a QD with arbitrary shape and with cubic crystal lattice can be written in the Bloch function basis

$$\mathbf{u}_6=\{|X\uparrow\rangle,|Y\uparrow\rangle,|Z\uparrow\rangle,|X\downarrow\rangle,|Y\downarrow\rangle,|Z\downarrow\rangle\} \qquad (8)$$

as[41]

$$\hat{H}_6=\begin{pmatrix}\hat{H}_3 & 0 \\ 0 & \hat{H}_3\end{pmatrix}+\hat{H}_{SO}. \qquad (9)$$

Hereafter we take the negative hole energy as positive. The operator $\hat{H}_3$ in the first term of Eq. (9) is the three-band hole Hamiltonian in the Bloch function basis

$$\mathbf{u}_3=\{|X\rangle,|Y\rangle,|Z\rangle\}. \qquad (10)$$

As seen from Eqs. (9)–(13) in case of zero spin-orbit coupling $(\Delta=0)$, the eigenstates of the Hamiltonian (9) are the twofold spin degenerate states of the Hamiltonian $\hat{H}_3$. The latter Hamiltonian has the form

$$\hat{H}_3=\frac{1}{2m_0}\begin{pmatrix}L\hat{p}_x^2+M\hat{p}_{\perp x}^2 & N\hat{p}_x\hat{p}_y & N\hat{p}_x\hat{p}_z \\ N\hat{p}_x\hat{p}_y & L\hat{p}_y^2+M\hat{p}_{\perp y}^2 & N\hat{p}_y\hat{p}_z \\ N\hat{p}_x\hat{p}_z & N\hat{p}_y\hat{p}_z & L\hat{p}_z^2+M\hat{p}_{\perp z}^2\end{pmatrix}, \qquad (11)$$

where $\hat{\mathbf{p}}=-i\hbar\nabla$ and $\hat{p}_{\perp i}^2=\hat{p}^2-\hat{p}_i^2$ $(i=x,y,z)$. Luttinger effective-mass parameters L, M, and N from Eq. (11) can be determined by fitting the energy bands near the valence band top with those calculated by the empirical pseudopotential method as in Ref. 43. The second term in Eq. (9) is the spin-orbit Hamiltonian

$$\hat{H}_{SO}=\begin{pmatrix}\hat{H}_{SO}^{(1)} & \hat{H}_{SO}^{(2)} \\ \hat{H}_{SO}^{(2)\dagger} & \hat{H}_{SO}^{(1)*}\end{pmatrix}, \qquad (12)$$

where

$$\hat{H}_{SO}^{(1)}=\frac{\Delta}{3}\begin{pmatrix}1 & i & 0 \\ -i & 1 & 0 \\ 0 & 0 & 1\end{pmatrix}, \hat{H}_{SO}^{(2)}=\frac{\Delta}{3}\begin{pmatrix}0 & 0 & -1 \\ 0 & 0 & i \\ 1 & -i & 0\end{pmatrix}, \qquad (13)$$

and Δ is the spin-orbit splitting energy.

Since the spin-orbit splitting energy in CdS is small ($\Delta=70$ meV), it is convenient to obtain the eigenstates of the Hamiltonian (9) in the following way. First, eigenenergies E_{3,a_0} and eigenfunctions Ψ_{3,a_0} of the three-band Hamiltonian (11) are numerically computed for a tetrahedral QD with a

certain dimension $a=a_0$ using the finite difference method described above for the calculation of electron states. Similarly to electron energy levels, three-band hole energy levels can be one fold, two fold, or three fold degenerate. Eigenstates for a QD with an arbitrary dimension a can be found using the size dependencies given by Eqs. (6) and (7) for electron states. Second, eigenenergies $E_{6,a}$ and eigenfunctions $\Psi_{6,a}$ of the six-band Hamiltonian (9) are computed by expanding six-band wave functions in terms of three-band wave functions as

$$\Psi_{6,a}(\mathbf{r}) = \left(\frac{a_0}{a}\right)^{3/2} \sum_{\mathbf{n},\sigma} A_{\mathbf{n},\sigma}(a) \Psi_{3,a_0}^{\mathbf{n}}\left(\frac{a_0}{a}\mathbf{r}\right)|\sigma\rangle, \quad (14)$$

where $A_{\mathbf{n},\sigma}(a)$ are the expansion coefficients, the set of quantum numbers of three-band states is denoted as $\mathbf{n}$, and σ is the spin of the missing electron. Considering the symmetry of the Hamiltonian $\hat{H}_6$, it can be shown, that hole states are either two fold or four fold degenerate. The notation n_λ, where $\lambda = 2$ or 4 is the degeneracy and $n=1,2,\ldots$, is the ordinal number of a level with given λ, is used to label hole energy levels.

The main benefit of using the described in the previous paragraph approach to obtain six-band hole states as a function of QD size is that the computationally intensive calculation of eigenvalues and eigenvectors of the Hamiltonian matrix is performed only one time, i.e., for a certain QD size. While three-band envelope wave functions $\Phi_{3,i}$ of

$$\Psi_3 = \sum_{i=1}^{3} \Phi_{3,i}u_{3,i} \quad (15)$$

can be chosen real valued, six-band envelope wave functions $\Phi_{6,i}$ of

$$\Psi_6 = \sum_{i=1}^{6} \Phi_{6,i}u_{6,i} \quad (16)$$

are essentially complex valued. Therefore, the direct calculation of six-band hole states would require dealing with a $6\mathcal{N}\times 6\mathcal{N}$ complex matrix instead of $3\mathcal{N}\times 3\mathcal{N}$ real matrix for three-band hole states.

B. Potential energy of the electron-hole system

Coulomb potential energy of the electron-hole system for a nanostructure with spatially modulated dielectric constant $\epsilon(\mathbf{r})$ is

$$U(\mathbf{r}_e,\mathbf{r}_h) = V_{\text{int}}(\mathbf{r}_e,\mathbf{r}_h) + V_{s\text{-}a}(\mathbf{r}_e) + V_{s\text{-}a}(\mathbf{r}_h). \quad (17)$$

In Eq. (17), $V_{\text{int}}(\mathbf{r}_e,\mathbf{r}_h)$ is the electron-hole interaction energy; it can be found from the Poisson equation

$$\nabla_{\mathbf{r}_h}\epsilon(\mathbf{r}_h)\nabla_{\mathbf{r}_h}V_{\text{int}}(\mathbf{r}_e,\mathbf{r}_h) = \frac{e}{\epsilon_0}\rho(\mathbf{r}_e,\mathbf{r}_h), \quad (18)$$

where $\rho(\mathbf{r}_e,\mathbf{r}_h)$ is the charge density at the point $\mathbf{r}_h$ of an electron with the coordinate $\mathbf{r}_e$. Second and third terms in the right-hand side of Eq. (17) are electron and hole self-action energies, respectively; they are defined as

$$V_{s\text{-}a}(\mathbf{r}) = -\frac{1}{2}\lim_{\mathbf{r}'\to\mathbf{r}}[V_{\text{int}}(\mathbf{r},\mathbf{r}') - V_{\text{int}}^B(\mathbf{r},\mathbf{r}')], \quad (19)$$

where $V_{\text{int}}^B(\mathbf{r}_e,\mathbf{r}_h)$ is the solution of the Poisson equation (18) in the left-hand side of which function $\epsilon(\mathbf{r}_h)$ is replaced with $\epsilon(\mathbf{r}_e)$, i.e., it is the local bulk solution of Eq. (18). Further, Eq. (18) is addressed to QD's with the dielectric constant equal to ε inside the QD and ε' outside the QD.

1. Spherical QD

In the electrostatic case, the charge density $\rho(\mathbf{r}_e,\mathbf{r}_h)$ is given by

$$\rho(\mathbf{r}_e,\mathbf{r}_h) = e\,\delta(\mathbf{r}_e - \mathbf{r}_h), \quad (20)$$

where $\delta(\mathbf{r})$ is the Dirac delta function. Therefore, the local bulk solution of Eq. (18) is

$$V_{\text{int}}^B(\mathbf{r}_e,\mathbf{r}_h) = -\frac{e^2}{4\pi\epsilon_0\epsilon(\mathbf{r}_e)|\mathbf{r}_e - \mathbf{r}_h|}. \quad (21)$$

Equation (18) can be solved almost analytically for a spherical QD. Since both electron and hole are confined inside the QD of radius R, only solution for $r_e < R$ and $r_h < R$ is presented:

$$V_{\text{int}}(\mathbf{r}_e,\mathbf{r}_h) = V_{\text{int}}^B(\mathbf{r}_e,\mathbf{r}_h) - \frac{e^2(\varepsilon - \varepsilon')}{4\pi\epsilon_0\varepsilon R}\sum_{l=0}^{\infty} P_l\left(\frac{\mathbf{r}_e\mathbf{r}_h}{r_e r_h}\right)$$
$$\times\frac{l+1}{(l+1)\varepsilon' + l\varepsilon}\left(\frac{r_e r_h}{R^2}\right)^l, \quad (22)$$

where $P_l(x)$ is the Legendre polynomial of order l. Substitution of Eq. (22) into Eq. (19) gives the self-action energy for $r < R$:

$$V_{s\text{-}a}(\mathbf{r}) = \frac{e^2(\varepsilon - \varepsilon')}{8\pi\epsilon_0\varepsilon R}\sum_{l=0}^{\infty}\frac{l+1}{(l+1)\varepsilon' + l\varepsilon}\left(\frac{r}{R}\right)^{2l}. \quad (23)$$

As seen from Eqs. (22) and (23) in the absence of the dielectric mismatch ($\varepsilon' = \varepsilon$), the electron and hole self-action energies are zero, and the electron-hole interaction energy takes its bulk value. Considering Eq. (17), one can notice that the part of $V_{\text{int}}(\mathbf{r}_e,\mathbf{r}_h)$ given by the second term in the right-hand side of Eq. (22) and the sum $V_{s\text{-}a}(\mathbf{r}_e) + V_{s\text{-}a}(\mathbf{r}_h)$ have opposite signs and, on average, close absolute values. This fact greatly reduces the influence of the dielectric mismatch on the Coulomb potential energy of the electron-hole system, making this energy close to its bulk value given by Eq. (21).

2. Tetrahedral QD

Among nonspherical QD's, a partially analytical solution of Eq. (18) can be found for a cubic QD.[44] For an arbitrary QD shape, in our case for tetrahedral one, Eq. (18) can be solved only numerically. The finite difference method on a composite grid is applied to solve the Poisson equation (18): the differential equation (18) is transformed into a system of linear equations which is solved iteratively.

The composite grid is constructed as follows. (i) a uniform grid with step length Λ/N' is introduced in the cube with edge $\Lambda > 2a$ [the dashed cube from Fig. 1 uniformly stretched by a factor $\Lambda/(2a)$]. The uniform grid has $(N'+1)^3$ nodes, including those on the cube's facets. (ii) A uniform grid with step length $2\Lambda/N'$ is introduced in the cube with edge 2Λ (the previous cube uniformly stretched by a factor 2). The latter grid adds $(N'+1)^3 - (N'/2+1)^3$ new nodes to the former one, resulting in a composite grid with $2(N'+1)^3 - (N'/2+1)^3$ nodes. (iii) Step (ii) is repeated until the composite grid with $(N'+1)^3 + (K-1)[(N'+1)^3 - (N'/2+1)^3]$ nodes is constructed in the cube with edge $K\Lambda$. After the appropriate boundary conditions are applied at the facets of the final cube (even zero boundary conditions work well if $K\Lambda \gg 2a$), the number of remaining nodes, and consequently, the order of the resulting linear system is $\mathcal{N}' = (N'-1)^3 + (K-1)[(N'+1)^3 - (N'/2+1)^3]$. If one considered the uniform grid with step length Λ/N' in the cube with edge $K\Lambda$, the corresponding order of the linear system would be $(KN'-1)^3$, what is approximately K^2 times larger than $\mathcal{N}'$. Due to the long-range character of the Coulomb interaction, in order to find the exact Coulomb potential inside the QD, one has to consider the region about 10 times larger than the QD dimension, i.e., $K \approx 10$. The advantage of using the composite grid, as described here, is obvious.

The charge density $\rho(\mathbf{r}_e, \mathbf{r}_h)$ at the node $\mathbf{n}_h$ of an electron at the node $\mathbf{n}_e$ belonging to the kth level of the composite grid can be written, within the finite difference method, as $(k = 1, \ldots, K)$

$$\rho(\mathbf{n}_e, \mathbf{n}_h) = \begin{cases} e\left(\dfrac{N'}{k\Lambda}\right)^3, & \mathbf{n}_e = \mathbf{n}_h, \\ 0, & \mathbf{n}_e \neq \mathbf{n}_h. \end{cases} \qquad (24)$$

The electron-hole interaction energy $V_{\text{int}}(\mathbf{n}_e, \mathbf{n}_h)$ is evaluated using Eq. (18) with the charge density (24) for each node $\mathbf{n}_e$. It is easy to prove, that the correct self-action energy on the composite gride can be given by Eq. (19) in the form

$$V_{s\text{-}a}(\mathbf{n}) = -\frac{1}{2}[V_{\text{int}}(\mathbf{n},\mathbf{n}) - V_{\text{int}}^B(\mathbf{n},\mathbf{n})], \qquad (25)$$

where the local bulk solution $V_{\text{int}}^B(\mathbf{n},\mathbf{n})$ is found as described below Eq. (19).

As seen from Eqs. (17)–(19), the dependence of the Coulomb potential energy on the QD dimension a has the form

$$U_a(\mathbf{r}_e, \mathbf{r}_h) = \left(\frac{a_0}{a}\right) U_{a_0}\left(\frac{a_0}{a}\mathbf{r}_e, \frac{a_0}{a}\mathbf{r}_h\right). \qquad (26)$$

This fact, again, allows one to obtain the Coulomb potential energy for any value of dimension a by computing a single case $a = a_0$.

C. Exciton states and oscillator strengths

Electron and hole states and electron-hole potential energy described above are used here to find exciton states and their oscillator strengths. For conciseness, we consider only tetrahedral QD's. An analogous approach can be applied for

spherical QD's. The exciton Hamiltonian in the envelope function representation is written as

$$\hat{H}_{\text{exc}} = \hat{H}_e(\mathbf{r}_e) + \hat{H}_6(\mathbf{r}_h) + U(\mathbf{r}_e, \mathbf{r}_h), \qquad (27)$$

where $\hat{H}_e$, $\hat{H}_6$, and U are defined by Eqs. (1), (9), and (17), correspondingly. Exciton states are eigenstates of the equation

$$\hat{H}_{\text{exc}}\Psi_{\text{exc}} = E_{\text{exc}}\Psi_{\text{exc}}. \qquad (28)$$

Neglecting the electron-hole potential energy U in Eq. (27), the solution of Eq. (28) are electron-hole pair states

$$\Psi_{e\text{-}h}^{\mathbf{k},\sigma_e;\mathbf{n}}(\mathbf{r}_e, \mathbf{r}_h) = \langle S\sigma_e | \Phi_e^{\mathbf{k}}(\mathbf{r}_e)\Psi_6^{\mathbf{n}}(\mathbf{r}_h), \qquad (29)$$

where $\mathbf{k}$ and $\mathbf{n}$ denote the sets of quantum numbers of one-band electron and six-band hole states, respectively, σ_e is the electron spin, $\langle S|$ is the Bloch function with zero momentum, Φ_e is the electron envelope function, and Ψ_6 is the hole wave function given by Eqs. (16) and (8). As seen, the dielectric confinement contribution is not included in the definition (29) of the electron-hole pair states.

Oscillator strengths of the electron-hole pair states, averaged over the electron spin, can be calculated as

$$f_{e\text{-}h}^{\mathbf{k};\mathbf{n}} \propto \sum_{\sigma_e} \left| \int \delta(\mathbf{r}_e - \mathbf{r}_h)\hat{\mathbf{p}}_h\Psi_{e\text{-}h}^{\mathbf{k},\sigma_e;\mathbf{n}}(\mathbf{r}_e, \mathbf{r}_h)d\mathbf{r}_e d\mathbf{r}_h \right|^2, \quad (30)$$

where $\hat{\mathbf{p}}_h \equiv -i\hbar\boldsymbol{\nabla}_{\mathbf{r}_h}$ is the hole momentum. Substituting Eqs. (7) and (14), (15) into Eqs. (29), (30) and taking into account relations $\langle \sigma_e | \sigma_h \rangle = \delta_{\sigma_e, \sigma_h}$ and

$$\langle S|\hat{p}_i|u_{3,j}\rangle = P\delta_{i,j}, \quad (i,j = x,y,z; P = \text{const}) \qquad (31)$$

one obtains

$$f_{e\text{-}h}^{\mathbf{k};\mathbf{n}}(a) \propto \sum_{\sigma,i} \left| \sum_{\mathbf{n}'} A_{\mathbf{n}',\sigma}^{\mathbf{n}}(a) \int \Phi_{e,a_0}^{\mathbf{k}}(\mathbf{r})\Phi_{3,a_0,i}^{\mathbf{n}'}(\mathbf{r})d\mathbf{r} \right|^2. \tag{32}$$

Since the electron-hole overlap integrals in Eq. (32) are taken at a fixed value of QD dimension $a = a_0$, the dependence of oscillator strengths on a comes from the size-dependent expansion coefficients $A_{\mathbf{n},\sigma}$ of the hole wave function (14).

The exciton wave function can be expanded in terms of wave functions of electron-hole pair states (29) as

$$\Psi_{\text{exc}}^{\sigma_e} = \sum_{\mathbf{k},\mathbf{n}} B_{\mathbf{k},\mathbf{n}}\Psi_{e\text{-}h}^{\mathbf{k},\sigma_e;\mathbf{n}}. \qquad (33)$$

Substituting Eq. (33) into Eq. (28) and taking into account Eq. (27) one can rewrite equation (28) in the following matrix representation:

$$\sum_{\mathbf{k},\mathbf{n}} H_{\mathbf{k},\mathbf{n}}^{\mathbf{k}',\mathbf{n}'} B_{\mathbf{k},\mathbf{n}} = E_{\text{exc}} B_{\mathbf{k}',\mathbf{n}'}, \qquad (34)$$

where the Hamiltonian matrix has the form

TABLE I. Parameters of cubic CdS: E_g: band gap; Δ: spin-orbit splitting; m_e: effective electron mass; ε: dielectric constant; L, M, and N: Luttinger parameters; γ_1, γ: Luttinger parameters and m_{lh}, m_{hh}: light and heavy hole masses in the spherical approximation (Ref. 41) (ε' - dielectric constant of H_2O).

E_g, eV	Δ, eV	ε	ε'
2.5 (Ref. 34)	0.07 (Ref. 45)	5.5 (Ref. 34)	1.78 (Ref. 34)
m_e, m_0	L	M	N
0.2 (Ref. 34)	4.863 [a]	1.064 [a]	5.633 [a]
γ_1	γ	m_{lh}, m_0	m_{hh}, m_0
2.330 [b]	0.817 [b]	0.252 [c]	1.434 [c]

[a]As in Ref. 43, parameters L, M, and N have been determined by fitting the energy bands near the valence band top with those calculated by the empirical pseudopotential method [form factors of cubic CdS have been taken from Refs. 46 and 47; lattice constant of cubic CdS is 0.582 nm (Ref. 33); reciprocal lattice vector has been restricted to $G^2 \leq 28$].

[b]Parameters γ_1 and γ have been calculated from L, M, and N using relations $\gamma_1 = (L + 2M)/3$ and $\gamma = (2(L - M) + 3N)/30$.

[c]Parameters m_{lh} and m_{hh} have been calculated from γ_1 and γ using relations $m_{lh} = m_0/(\gamma_1 + 2\gamma)$ and $m_{hh} = m_0/(\gamma_1 - 2\gamma)$. Values of these parameters are close to hole masses for cubic CdS studied in Ref. 40.

$$H_{\mathbf{k,n}}^{\mathbf{k',n'}} = (E_e^{\mathbf{k}} + E_6^{\mathbf{n}}) \delta_{\mathbf{k,k'}} \delta_{\mathbf{n,n'}} + U_{\mathbf{k,n}}^{\mathbf{k',n'}}, \qquad (35)$$

and $U_{\mathbf{k,n}}^{\mathbf{k',n'}}$ is the matrix of the electron-hole potential energy U constructed on the basis functions $\Psi_{e\text{-}h}^{\mathbf{k},\sigma_e;\mathbf{n}}$. The form of the Hamiltonian matrix for any value of dimension a can be obtained from Eq. (35) for $a = a_0$ if one multiplies the first term in the right-hand side of Eq. (35) by $(a_0/a)^2$ [according to Eq. (6)], multiplies the second term by (a_0/a) [according to Eq. (26)], and replaces the expansion coefficients $A_{\mathbf{n},\sigma}(a_0)$, defining hole wave functions (14), by $A_{\mathbf{n},\sigma}(a)$.

The oscillator strength $f_{\text{exc}}^{\mathbf{m}}$ for an exciton level $\mathbf{m}$ is calculated using Eq. (30) where $\Psi_{e\text{-}h}^{\mathbf{k},\sigma_e;\mathbf{n}}$ is replaced by $\Psi_{\text{exc}}^{\mathbf{m},\sigma_e}$ given by Eq. (33). At the same time, Eq. (32) remains valid if one replaces $A_{\mathbf{n'},\sigma}^{\mathbf{n}}(a)$ by $\Sigma_{\mathbf{n}} B_{\mathbf{k,n}}^{\mathbf{m}}(a) A_{\mathbf{n'},\sigma}^{\mathbf{n}}(a)$ and sums the expression under the absolute value sign over $\mathbf{k}$.

III. NUMERICAL RESULTS AND DISCUSSION

Parameters employed for the calculation of electron, hole, and exciton states in tetrahedral and spherical CdS QD's are listed in Table I. The calculation of electron and hole states in tetrahedral and spherical QD's has been carried out according to Sec. II A. In order to find electron and three-band hole states in a tetrahedral QD, the grid with step length $2a/60$ has been used. 20 lowest electron states and 43 lowest hole states (including degeneracy) have been computed using the matrix electron Hamiltonian of order $\mathcal{N} = 68\,499$ and the matrix three-band hole Hamiltonian of order $3\mathcal{N} = 205\,497$ correspondingly.

In the upper part of Fig. 2, wave functions of the three lowest electron states are shown. Among those states, $e1$ and
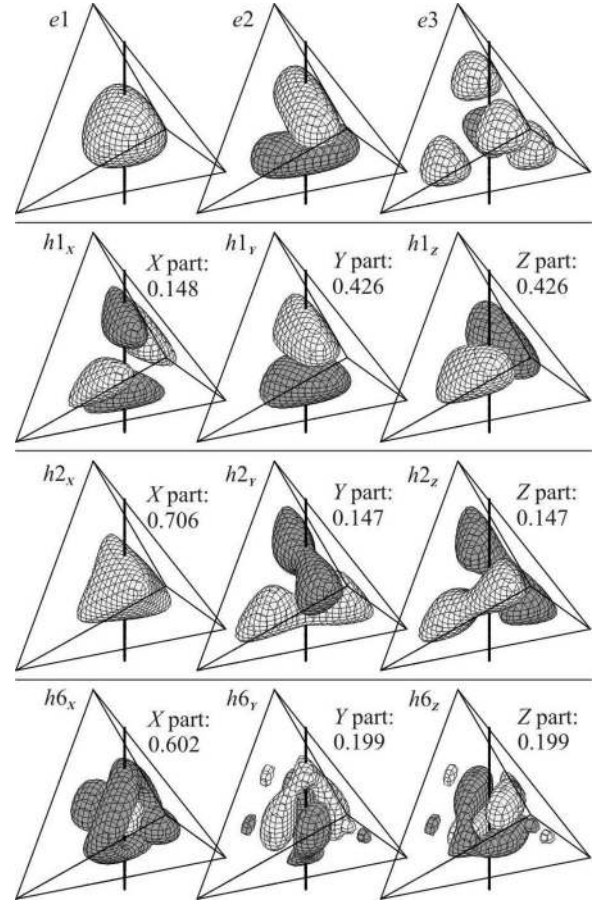

FIG. 2. $e1$, $e2$, $e3$ electron and $h1$, $h2$, $h6$ hole wave functions calculated within one and three band models correspondingly. Light and dark colors denote positive and negative values of the wave function. Each electron wave function is represented by the isosurface of the probability density $p_e = 0.8$. Each of three components of hole wave functions is represented by the isosurface of the probability density $p_{h_X} = p_{h_Y} = p_{h_Z} = 0.8$ of the particular wave function component. The relative contribution of all three hole components to the integral probability density is indicated near each wave function component.

$e3$ are nondegenerate and $e2$ is threefold degenerate. In the rest of Fig. 2, X, Y, and Z components of the wave functions of threefold degenerate lowest hole states $h1$, $h2$ and the state $h6$ are presented. Our choice of the Bloch function basis (10) is convenient for tetrahedral QD's, because it allows us to choose and present one such particular three-band wave function of a triply degenerate state, that two other three-band wave functions can be easily found from the symmetry considerations. It should be noted, that while the wave function $e1$ of electron ground state is fully symmetrical, a fully symmetrical component does not enter the hole ground state $h1$ and appears only in $h2$ ($h2_X$). 20 lowest electron energy levels for tetrahedral, cubical,[44] and spherical CdS QD's are listed in Table II as a function of QD volume. It is seen that the electron ground state energy as well as interlevel distances decrease in the sequence of QD's with equal volumes: tetrahedral $\rightarrow$ cubical $\rightarrow$ spherical. It is also seen, that interlevel distances in QD's with equal ground state en-

TABLE II. First 20 electron energy levels (including degeneracy) in tetrahedral, cubical, and spherical CdS QD's. The degeneracy is indicated for each level. Electron ground state energy (meV) as a function of the QD volume (nm^3) is calculated for different QD shapes as $E_1^{tetr}(V) = 6905.72/V^{2/3}$, $E_1^{cub}(V) = 5641.09/V^{2/3}$, and $E_1^{sph}(V) = 4886.16/V^{2/3}$.

n	E_n^{tetr}/E_1^{tetr}		E_n^{cub}/E_1^{cub}		E_n^{sph}/E_1^{sph}	
1	1.000 00	×1	1.000 00	×1	1.000 00	×1
2	1.844 26	×3	2.000 00	×3	2.045 75	×3
3	2.759 52	×1	3.000 00	×3	3.365 63	×5
4	2.927 86	×3	3.666 67	×3	4.000 00	×1
5	3.057 66	×2	4.000 00	×1	4.947 63	×7
6	4.015 24	×3	4.666 67	×6	6.046 80	×3
7	4.209 20	×1	5.666 67	×3		
8	4.363 15	×3				
9	4.532 92	×3				

ergies increase, on average, and the highest order of degeneracy rises in the aforementioned sequence.

Using the wave functions of the three-band hole Hamiltonian found above, 86 states of the six-band Hamiltonian are computed as given by Eq. (14) for all required values of the QD dimension a. In Figs. 3(a) and 3(b), hole energy levels, calculated within the six-band model, are depicted for spherical QD's as a function of R and for tetrahedral QD's as a function of a, respectively. The hole energy is counted from the lowest state containing a fully symmetrical component: $1S_{3/2}$ for spherical QD's and 1_4 for tetrahedral QD's (the dependence of the reference level on the corresponding dimension is indicated in inserts). Level labeling has been described in Sec. II A.

The size quantization of an electron in CdS QD's is much stronger than that of a hole. This fact is related to the complex structure of the valence band as well as with the values of the effective-mass parameters. Thus, in the case of tetra-

hedral CdS QD, the energy interval between the 1st and 86th hole levels is two times narrower than the energy interval between the 1st and 2nd electron levels. The latter leads to the conclusion that inclusion of the electron ground state only is enough to describe main optical transitions in CdS QD's.

The oscillator strengths (see Sec. II C) of electron (ground state)-hole pairs are shown in Figs. 3(c) and 3(d) for spherical and tetrahedral QD's correspondingly. Hole levels with nonzero oscillator strengths are depicted in Figs. 3(a) and 3(b) with thick curves. One of the substantial differences in the hole energy spectra of spherical and tetrahedral QD's is that the hole ground state is always optically passive in spherical QD's and, on the contrary, optically active in tetrahedral QD's. In conformity with Eq. (32), the dependence of oscillator strengths on the QD size is a consequence of the nonzero value of the spin-orbit splitting energy Δ in CdS. It is interesting that the optical activity of the hole ground state in tetrahedral QD raises with increasing of the QD dimension a.

The electron-hole potential energy (17) in spherical and tetrahedral QD's has been calculated according to Sec. II B. A composite grid with parameters $\Lambda = 2.4a$, $N' = 36$, and $K = 5$ has been employed to calculate the potential energy in tetrahedral QD's. While the resulting step length in the QD region is $2a/30$, i.e., twice coarser than the step length used in the calculation of electron and hole states, the volume of the considered space region is 648 times larger than the QD volume. Discretization of the Poisson equation (18) on the described grid leads to the linear system of order $\mathcal{N}' = 218\,051$. This system should have been solved for each node $\mathbf{n}_e$ inside the tetrahedron, i.e., 8149 times.

Since for the investigation of optical transitions and for the calculation of exciton states in QD's we should be concerned only with the electron ground state, the matrix element of the electron-hole potential energy $U_{\mathbf{k,n}}^{\mathbf{k',n'}}$ from Eq.
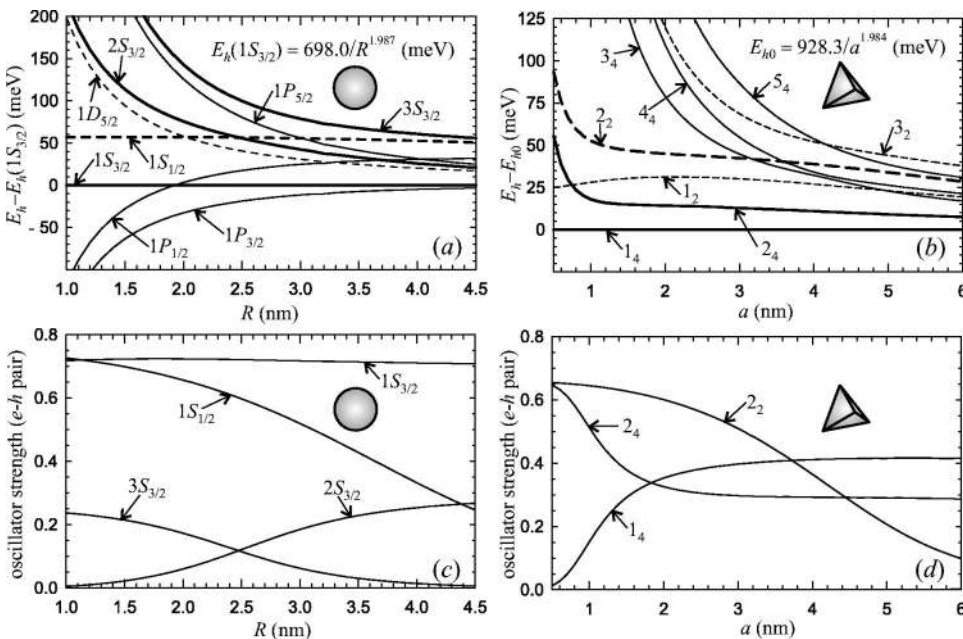

FIG. 3. Quantum confinement hole energy levels (upper panels) and oscillator strengths of some electron-hole pair states (lower panels) for spherical [panels (a) and (c)] and tetrahedral [panels (b) and (d)] QD's as a function of their dimensions. Thick curves in panels (a) and (b) represent hole states corresponding to electron (ground state)-hole pairs with nonzero oscillator strengths shown in panels (c) and (d), respectively.
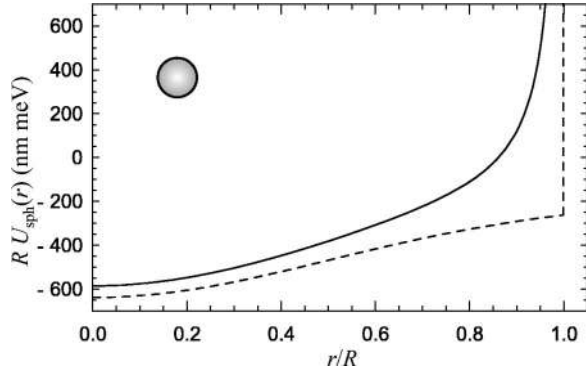
FIG. 4. Coulomb potential energy of the electron-hole system for a spherical QD averaged over the wave function of an electron in the ground state. Solid curve denotes the sum of the Coulomb energy of the electron-hole interaction accounting for the dielectric mismatch between the QD and the surrounding media and of electron and hole self-action energies. Dashed curve denotes the bulk Coulomb energy with the dielectric constant of the QD (vertical dashed line indicates the confinement potential energy).

(35) reduces to $U_{0,\mathbf{n}}^{0,\mathbf{n}'}$. The latter fact can be thought as a hole confined in a potential well $U(\mathbf{r}_h)$ created by an electron in the ground state and by the dielectric mismatch. This potential well is the electron-hole potential energy (17) averaged over the wave function of an electron in the ground state. There is no necessity to compute the electron-hole interaction energy $V_{\text{int}}(\mathbf{r}_e, \mathbf{r}_h)$ for each value of $\mathbf{r}_e$ and later, when averaging Eq. (17), to average $V_{\text{int}}(\mathbf{r}_e, \mathbf{r}_h)$ over $\mathbf{r}_e$. It is much simpler to average Eq. (18) over the wave function of an electron in the ground state and then to solve it with respect to the averaged potential energy $U(\mathbf{r}_h)$. Unfortunately, there is no such simplification for the calculation of the self-action energy $V_{s-a}(\mathbf{r})$ and it is still necessary to solve the linear system of 218 051 equations 8149 times (calculation of the self-action energy in tetrahedral QD's turned out to be the most tedious one).

The averaged potential energy $U(\mathbf{r}_h)$ is represented by solid curves in Figs. 4 and 5 for spherical and tetrahedral CdS QD's in H_2O correspondingly. Three solid curves in
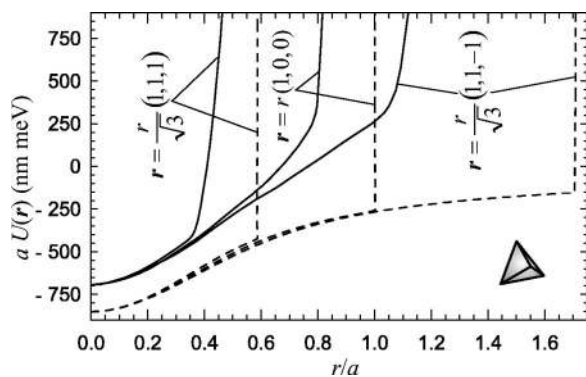

FIG. 5. The same as in Fig. 4, but for a tetrahedral QD. Three dashed and three solid curves indicate three different directions from the center of the tetrahedron: to the center of the face, to the middle of the edge, and to the vertex (from left to right).

Fig. 5 show the potential energy profile along three main directions of a tetrahedron. Dashed curves in Figs. 4 and 5 give the averaged potential energy $U(\mathbf{r}_h)$ in the absence of the dielectric mismatch at the QD boundary, namely, when $\varepsilon' = \varepsilon$. It is seen that even in our case where $\varepsilon/\varepsilon' \sim 3$, the potential energy $U(\mathbf{r}_h)$ does not differ significantly from the case $\varepsilon' = \varepsilon$ (the reasons of such behavior have been indicated at the end of Sec. II B 1 and discussed in Ref. 48). As also seen from the figures, the dielectric mismatch effect diminishes the effective size of QD's. Comparing Figs. 4 and 5 one can see that due to the complicate shape of the QD boundary, the aforementioned diminishing is more pronounced in tetrahedral QD's. This fact should have a strong effect on the electron-hole pair states in tetrahedral QD's.

Exciton states and their oscillator strengths for spherical and tetrahedral QD's have been calculated according to Sec. II C. For spherical QD's, as far as we are concerned with only spherically symmetric electron ground state and the averaged potential $U(\mathbf{r}_h)$ is also spherically symmetric, exciton states have the same set of quantum numbers as hole states. Analogously, because electron ground state and the averaged potential $U(\mathbf{r}_h)$ are tetrahedrally symmetric in tetrahedral QD's, the sets of quantum numbers in such QD's are the same for hole and exciton states. To obtain exciton states in tetrahedral QD's, we have used 86 coefficients $B_{0,\mathbf{n}}$ in the sum (33), i.e., all calculated hole states have been taken into account.

In Figs. 6(a) and 6(b), exciton energy levels are shown as a function of the QD size for spherical and tetrahedral QD's, correspondingly. The exciton energy is counted from the lowest exciton state containing a fully symmetrical component. The dependence of the reference energies for both QD's on the QD size is given in insets (here, as well as in inserts to Figs. 3, 7, and 8, coefficients in the analytical expressions are fitted using the least squares method). Different types of curves in Figs. 6(a) and 6(b) correspond to the same types of curves in Figs. 3(a) and 3(b). In Figs. 6(c) and 6(d), nonzero oscillator strengths for exciton states in spherical and tetrahedral QD's respectively are depicted as a function of QD size. Corresponding energy levels are represented in Figs. 6(a) and 6(b) with thick curves.

Exciton energy levels in spherical and tetrahedral QD's are resembling to a considerable degree. For instance, exciton ground states 1_4 in tetrahedral QD's with any a and $1S_{3/2}$ in spherical QD's with $R > 1.35$ nm have a fully symmetrical component. Another similar feature is the presence of an exciton level ($1S_{1/2}$ for spherical QD's and 1_2 for tetrahedral QD's) equidistant from the exciton ground state for any QD size. The aforementioned pair of energy levels as well as ground state energy levels in both QD's have also a similar dependence of their oscillator strengths on the QD size. The above facts allow one to conclude that the self-action potential energy diminishes the effective size of the tetrahedron in such way, that it looks similar to a tetrahedrally deformed sphere. In fact, the distance between three vertical dashed lines in Fig. 5 (real boundaries of the tetrahedron) is larger than the distance between three almost vertical parts of solid lines, which show an effective QD size.

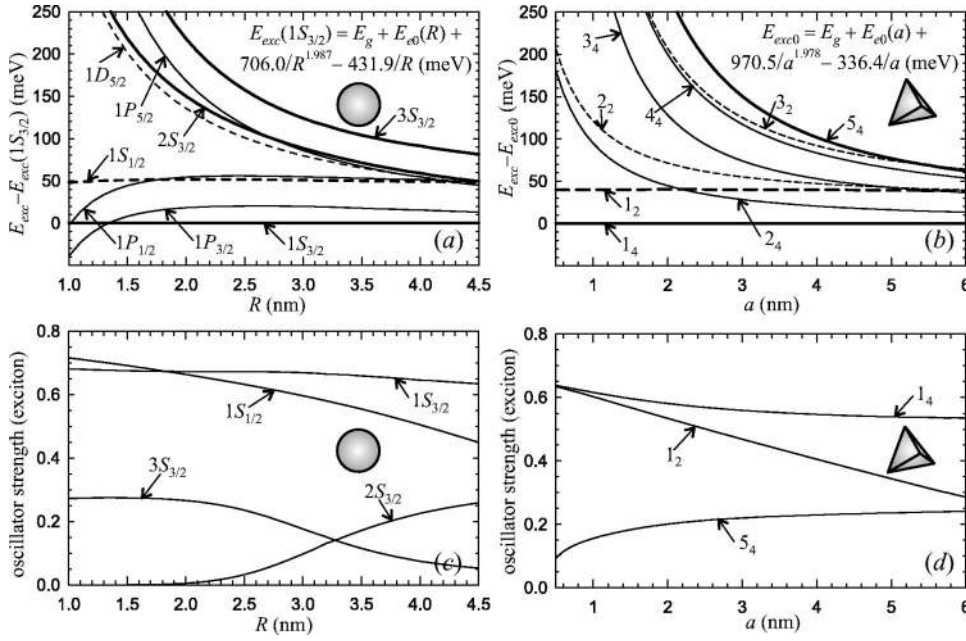Hole energy levels in Figs. 3(a) and 3(b) can be thought

FIG. 6. Exciton energy levels (upper panels) and oscillator strengths of some exciton states (lower panels) for spherical [panels (a) and (c)] and tetrahedral [panels (b) and (d)] QD's as a function of their dimensions. Thick curves in panels (a) and (b) represent exciton states with non-zero oscillator strengths shown in panels (c) and (d), respectively. Different types of curves in panels (a) and (b) originate from the same types of curves that represent hole states in Figs. 3(a) and 3(b), correspondingly. In the inserts, E_g is the bulk CdS gap energy and E_{e0} is the quantum confinement electron ground state energy.

as electron-hole pair levels without the dielectric confinement contribution if the bulk CdS gap and the electron ground state energies are considered added to the hole reference energy. Therefore, comparing Figs. 3 and 6, one can arrive at the following conclusions about the influence of the Coulomb potential energy of the electron-hole system on the exciton spectra in spherical and tetrahedral QD's: (i) in spherical QD's, the relative position of levels changes; it is also seen that optically active exciton states become energetically more favorable than optically inactive ones, (ii) in tetrahedral QD's, electron-hole pair states mix essentially when forming exciton states which in their turn tend to reproduce the picture of exciton states in spherical QD's, (iii) in both QD's, a regularity is observed that the exciton ground state

has large oscillator strength which is practically unchanged with varying the QD size.

In the spherical six-band hole Hamiltonian used to calculate hole states in spherical QD's, the Luttinger parameters obey the condition $\gamma_2 = \gamma_3 \equiv \gamma$. However, using parameters from Table I, one can obtain that $\gamma_2 = (L - M)/6 = 0.633$ and $\gamma_3 = N/6 = 0.939$ are different. Therefore, one can expect that the difference between γ_2 and γ_3 will result in small corrections to the hole and exciton spectra in spherical QD's, for example, some degenerate in case $\gamma_2 = \gamma_3$ levels can split due to the reduction of the Hamiltonian symmetry from spherical to cubical. It has been checked, however, that no substantial changes occurs in the degeneracy and relative position of lowest hole levels when the case $\gamma_2 \neq \gamma_3$ is considered. On these grounds one can conclude that all similarities and distinctions revealed in the spectra of spherical and tetrahedral QD's are not connected with the accepted approximation to calculate hole states, but are ruled by the QD shape.

We have specially considered the influence of the dielectric mismatch at the QD boundary on the binding energy of the exciton ground state in spherical and tetrahedral QD's.
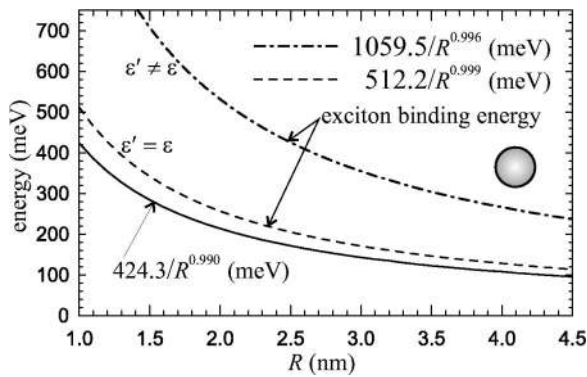

FIG. 7. Binding energy of the exciton ground state in a spherical QD calculated using the Coulomb potential energy accounting for the dielectric mismatch between the QD and the surrounding media as well as for the self-action energy of an electron and a hole (dash-dotted line) and using the bulk Coulomb potential energy with the dielectric constant of the QD (dashed line). The difference between the quantum confinement gap energy and the exciton gap energy is plotted with the solid curve. The distance between the solid and dash-dotted curves shows the sum of dielectric confinement contributions to electron and hole energies.
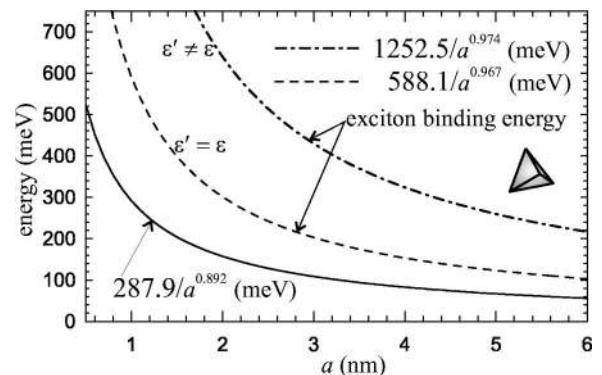

FIG. 8. The same as in Fig. 7, but for a tetrahedral QD.

Using Eq. (17), Eq. (27) can be rewritten in the form

$$\hat{H}_{exc} = [\hat{H}_e(\mathbf{r}_e) + V_{s-a}(\mathbf{r}_e)] + [\hat{H}_6(\mathbf{r}_h) + V_{s-a}(\mathbf{r}_h)]$$
$$+ V_{int}(\mathbf{r}_e, \mathbf{r}_h). \tag{36}$$

The definition of the exciton binding energy in QD's is $E_b = E_e + E_h - E_{exc}$, where the electron (hole) energy E_e (E_h) is the eigenenergy of the Hamiltonian in the first (second) parentheses in the right-hand side of Eq. (36) (see, for example, Ref. 39). This definition of the exciton binding energy includes the self-image effects in the single particle energies. Alternatively, the exciton binding energy can be defined as the difference between the single particle energies without the self-image effects and the exciton energy. Another definition will be just a different way of partitioning the exciton energy. As previously discussed, the electron (hole) energies can be written as $E_{e(h)} = E_{e(h)}^{QC} + \Delta E_{e(h)}^{DC}$. For spherical and tetrahedral QD's, E_e^{QC}, E_h^{QC}, and E_{exc} have been represented in Table II, Fig. 3, and Fig. 6 respectively. Since the calculation of $\Delta E_{e(h)}^{DC}$ is straightforward, we restrict ourselves with the description of the main results. When energies are measured in meV and dimensions are in nm, we have in spherical QD's: $\Delta E_e^{DC} = 326.7/R$ for the electron ground state energy and $\Delta E_h^{DC} = 308.5/R$ for the hole ground state energy and in tetrahedral QD's: $\Delta E_e^{DC} = 476.7/a$ and $\Delta E_h^{DC} = 487.3/a$ for the electron and hole ground states energies, correspondingly. It is interesting to note, that the picture of the lowest hole energy levels in their self-action potential resemble Fig. 3(a) for spherical QD's and Fig. 6(b) for tetrahedral QD's. This fact shows that the main reason of mixing the electron-hole pair levels from Fig. 3 into the exciton levels form Fig. 6 is the electron-hole interaction energy for spherical QD's and the hole self-action energy for tetrahedral QD's.

The exciton binding energy in spherical and tetrahedral QD's with the dielectric mismatch is shown with dash-dotted lines in Figs. 7 and 8, respectively. Solid lines in these figures represent the difference between the quantum confinement gap energy ($E_e^{QC} + E_h^{QC}$) and the exciton gap energy (E_{exc}) accounting for the dielectric mismatch (the potential plotted in Figs. 4 and 5 with solid lines has been used) and dashed lines represent the binding energy when the dielectric constant of the surrounding medium is equal to the dielectric constant of the QD (the potential plotted in Figs. 4 and 5 with dashed lines has been used). It is seen from Figs. 7 and 8 that the dielectric mismatch at the CdS/H_2O boundary leads to the enhancement of the exciton binding energy in both spherical and tetrahedral QD's by a factor of 2. The exciton binding energy consists of the direct Coulomb energy that does not depend on ε' (dashed curves) and the polarization contribution that depends strongly on ε' (the difference between dash-dotted and dashed curves). The polarization contribution to the exciton binding energy tends to cancel the dielectric confinement contributions to the electron and hole energies, what results in a weak dependence of the exciton gap energy on the dielectric environment.[48]

The exciton ground state energies as a function of QD size for spherical and tetrahedral CdS QD's calculated in the present work are compared in Fig. 9 with the results obtained
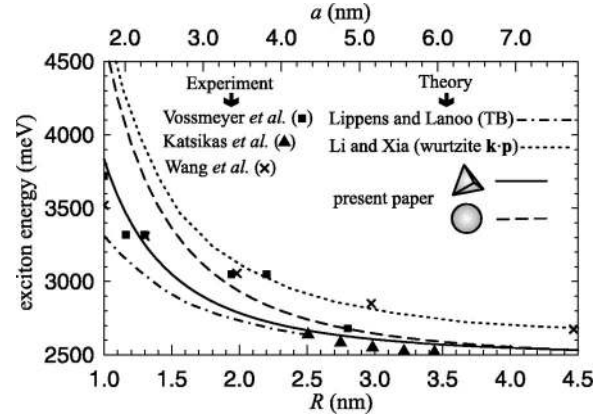

FIG. 9. Exciton ground state energy as a function of the radius R for spherical CdS QD's and as a function of the dimension a (see Fig. 1) for tetrahedral CdS QD's. For a given energy, R is the radius of a sphere inscribed in the tetrahedron with dimension a. Boxes (Ref. 21), triangles (Ref. 49), and crosses (Ref. 50) are the experimental points; dash-dotted curve is the result of a tight-binding calculation (Ref. 51); dotted curve is the result of a $\mathbf{k}\cdot\mathbf{p}$ calculation for wurtzite nanocrystals (Ref. 45). Solid and dashed curves are the theoretical results of the present paper for tetrahedral and spherical QD's correspondingly.

in recent theoretical and experimental studies. Solid and dashed curves in Fig. 9 represent our results for tetrahedral and spherical QD's, respectively. As seen, the exciton ground state energy E_{exc0} for a relatively large tetrahedral QD ($R > 3.5$ nm) is close to E_{exc0} for the spherical QD inscribed in the corresponding tetrahedron ($R = a/\sqrt{3}$). This fact can be explained if we note that the Coulomb potential energy of the electron-hole system in the central region of a relatively large tetrahedral QD (i.e. at the bottom of the potential well) almost coincides with this potential energy in the central region of the spherical QD inscribed in the tetrahedron (compare Figs. 5 and 4). The exciton ground state energy E_{exc0} in a relatively small tetrahedral QD is less than E_{exc0} in the spherical QD inscribed in the tetrahedron, because electron and hole densities penetrate substantially in the direction of edges and vertices of small tetrahedral QD's.

The dash-dotted curve in Fig. 9 represents the exciton ground state energy for spherical CdS QD's with $R < 2.5$ nm calculated in Ref. 51 using the tight-binding (TB) method for single particle electron and hole states and the potential energy of the electron-hole interaction for a bulk CdS crystal. For such small QD's, the TB method should give more accurate single particle electron and hole states than the $\mathbf{k}\cdot\mathbf{p}$ method used in this paper. However, as we have shown, the dielectric mismatch at the CdS boundary also cannot be neglected. The applicability of continuum macroscopic electrostatics for very small structures with sizes of only few unit cells has been proven in Refs. 52 and 53 taking into account the spatial variation of the dielectric constant. Figures 4 and 5 show that the dielectric mismatch at the CdS/H_2O boundary should increase the exciton ground state energy E_{exc0}. This can explain the fact that the values of E_{exc0} calculated in Ref. 51 are lower than the experimental values of Ref. 21 (boxes in Fig. 9).

Triangles in Fig. 9 represent the experimental points from Ref. 49 for CdS QD's with cubic crystal lattice. In the latter reference, the theoretical energies of exciton states calculated as in Ref. 54 are also presented. Despite the fact that Ref. 54 takes into account only one hole band, an excellent agreement with the experiment has been found for the exciton ground state. The one-band hole mass from Ref. 54 is $m_h = 0.8m_0$. Values of heavy and light hole masses within the six-band model considered in the present paper are listed in Table I. In the region 2.5 nm$<R<$3.5 nm, the six-band model gives the hole ground state energy, which is 1.5 times larger in absolute value than the corresponding result of the one-band estimation of Ref. 54. Since our accurate results for the exciton ground state energy are slightly larger than the experimental points of Ref. 49, the above better agreement with the calculation of Ref. 54 must be a result of the selection of the one-band hole mass.

Noticeable scattering of the experimental points from Ref. 21 is probably due to the uncertainties in the determination of the effective radius of tetrahedron-shaped QD's. The scattering can be also due to the fact that while the crystal structure for the smallest QD's was determined to be cubic and for the largest QD's it was found to be hexagonal (wurtzite), the crystal structure of other samples seemed to be neither cubic nor hexagonal. Crosses in Fig. 9 show the experimental points from Ref. 50 for wurtzite CdS QD's. The exciton ground state energy in wurtzite QD's is substantially higher than this energy in QD's with cubic crystal lattice. The dotted curve in Fig. 9 shows the result of the six-band $\mathbf{k} \cdot \mathbf{p}$ calculation[45] for wurtzite QD's by Li and Xia who did not take into account the dielectric mismatch.

Summarizing the results presented in Fig. 9, we can state that our exciton ground state energy in both spherical and tetrahedral QD's is close to the experimental data of Refs. 21 and 49 for CdS QD's with cubic crystal lattice. Comparing the theoretical results of different authors, it is seen that the TB calculation gives lower exciton ground state energy E_{exc0} and the $\mathbf{k} \cdot \mathbf{p}$ calculation for wurtzite QD's gives higher E_{exc0} than our $\mathbf{k} \cdot \mathbf{p}$ results that also take into account the dielectric mismatch at the QD boundary. Unlike other papers, our exciton states depend on the dielectric constant of the exterior medium, therefore, taking into account the exact dielectric environment of each particular experiment should bring our results closer to the corresponding experimental points.

The Stokes shift in CdS QD's has been observed in Ref. 49. At the same time, our calculation gives optically active exciton ground state. The situation here is similar to that in case of spherical InAs and CdTe QD's where the Stokes shift has been explained[55,56] employing the electron-hole spin-exchange interaction. This interaction splits the optically active exciton ground state into few states, the lowest of which is optically passive.

Calculated in the present work, exciton ground state energy as a function of QD size is only an approximation for QD's with $R<1.5$ nm since the penetration of the electron density into the exterior medium becomes substantial for such small QD's and, consequently, the hard wall boundary conditions for the electron wave function cannot work. How-ever, taking into account the finiteness of the potential barrier should lead to a better agreement with the experiment.

The $\mathbf{k} \cdot \mathbf{p}$ model is an extrapolation for the smallest QD's investigated in this paper, because the conception of the envelope wave function becomes dubious when the size of QD's is only few unit cells. However, the results obtained within the $\mathbf{k} \cdot \mathbf{p}$ model for such small QD's turn out to be close to the correct results. For example, the multiband $\mathbf{k} \cdot \mathbf{p}$ model can successfully describe[35,36] the distribution of electron and hole densities in QDQW's with only one-monolayer thick quantum well. Moreover, it has been found in Ref. 57 that the eight-band $\mathbf{k} \cdot \mathbf{p}$ model successfully describes the experimentally observed level structure and relative transition intensities in spherical InAs QD's down to about 1.2 nm in radius. Thus, we can conclude that the exciton states and optical transitions obtained in the present paper for spherical and tetrahedral QD's will not change noticeably if one uses another approach, such as TB. One can also say that in order to describe electron and hole states near the edges and vertices in the tetrahedral QD's, it is necessary to take into account high $\mathbf{k}$ states that are beyond the limits of the $\mathbf{k} \cdot \mathbf{p}$ model. On the other hand, as seen from Fig. 2 and from the fact that electron and hole ground states in large tetrahedral QD's almost coincide with those states in the inscribed in the tetrahedron sphere, electron and hole densities near the edges and vertices of the tetrahedron are extremely small. Another theory should not give any substantial corrections in this case as well.

One can see from Fig. 9, that the QD shape (spherical or tetrahedral) does not have any principal influence on the exciton ground state. In this connection it is interesting to consider next exciton states. Exciton energies of allowed optical transitions in spherical and tetrahedral CdS QD's counted from the exciton ground state energy E_{exc0} are plotted versus E_{exc0} in Fig. 10. Relative oscillator strengths of the optical transitions are represented by the size of the corresponding symbols. Due to the high symmetry of spherical QD's, the number of optically active exciton states is small (there are only four such states in Fig. 10). For tetrahedral QD's, in addition to the four states with large oscillator strengths, there are a lot of states with very small oscillator strength. It is seen that first two optically active exciton sates are similar in QD's of both shapes. The third and fourth exciton states with large oscillator strength are higher in energy for spherical QD's than they are for tetrahedral QD's. For small QD's, this difference in energies is of order of hundreds of millielectron-volts. This fact shows that optical transitions involving higher exciton states are different for spherical and tetrahedral QD's. Thus, we can conclude that having an experimental optical spectrum of a single QD and knowing the approximate dimensions of the QD, it is possible to estimate the shape of the QD. The knowledge of the QD shape in its turn enables a thorough theoretical investigation of other QD properties in the direction of their practical applications.

IV. CONCLUSIONS

A theory of electron, hole, and exciton states in spherical and tetrahedral CdS QD's has been developed. Exciton en-
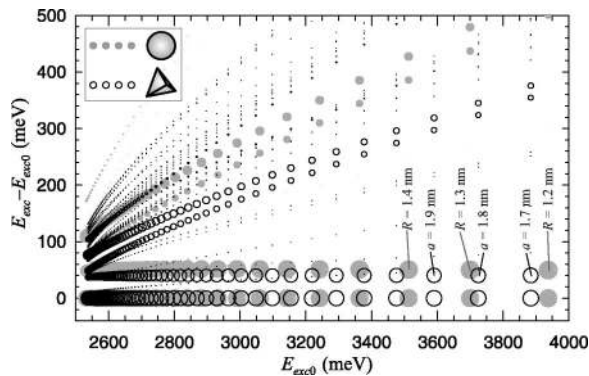
FIG. 10. Exciton energies of allowed optical transitions in spherical (gray disks) and tetrahedral (circles) CdS QD's counted from the exciton ground state energy E_{exc0} and plotted versus E_{exc0}. Relative oscillator strengths of the optical transitions are represented by the size of gray disks for spherical QD's and by the size of circles for tetrahedral QDs. The rightmost gray disks correspond to a QD with $R = 1.2$ nm and the rightmost circles correspond to a QD with $a = 1.7$ nm. Each next (from right to left) gray disk or circle represents the QD with a respective dimension (R or a) increased by 0.1 nm. Highest excitonic transitions in the region of lowest E_{exc0} have not been calculated.

ergy spectra have been calculated using the Coulomb potential energy of the electron-hole system accounting for the dielectric mismatch between the QD and the surrounding media as well as for the self-action energy of an electron and a hole. One-band electron and six-band hole wave functions and corresponding energy levels as well as the Coulomb potential energy in spherical QD's have been found analytically. For tetrahedral QD's, one-band electron and three-band hole states ($\Delta = 0$) as well as the Coulomb potential energy have been found numerically using the finite difference method. Six-band hole states ($\Delta \neq 0$) have been computed by expanding six-band wave functions in terms of three-band ones. Exciton wave functions in both QD's have been expanded in terms of wave functions of electron-hole pair states. Oscillator strengths of electron-hole pair and exciton energy levels have been calculated as a function of the QD size.

It has been shown that the aforementioned potential energy of the electron-hole system, averaged over the wave function of an electron in the ground state, in a tetrahedral QD forms a 3D potential well with the profile of a truncated tetrahedron with smoothed edges, i.e., a tetrahedrally deformed sphere. This effect can be explained by the increase of the self-action energy near the intersections of two or three face plains of the tetrahedron.

The lowest electron-hole pair energy is found to be optically passive in the spherical QD. This fact is known to lead to some difficulties in the theoretical interpretation of observed photoluminescence spectra. In contrast to spherical QD's, lowest electron-hole pair energies in tetrahedral QD's are optically active. The Coulomb potential energy influences the exciton spectrum in spherical QD's in such way that relative position of electron-hole pair levels changes and lowest optically active exciton states become energetically more favorable than optically inactive ones. Unlike electron-hole pair levels, exciton energy levels in spherical and tetrahedral QD's have many similar features. For example, exciton ground states in a tetrahedral QD of any size and in a spherical QD of almost any radii are optically active. The ground states in both QD's have large oscillator strengths which are practically unchanged with varying the QD size.

The dielectric mismatch at the CdS/H$_2$O boundary leads to the enhancement of the exciton binding energy by a factor of two in both spherical and tetrahedral QD's. Calculated exciton ground state energies for spherical and tetrahedral CdS QD's have been compared with the results obtained in recent theoretical and experimental studies. A satisfactory agreement with the experimental data has been found. A clear distinction in the optical properties of tetrahedral and spherical QD's has been revealed. In conclusion, we established that taking into account the real shape of the quantum dots and Coulomb potential energy with the dielectric mismatch at the QD boundary are essential for theoretical interpretation of exciton optical spectra.

*Electronic address: fonobero@yahoo.com; URL: http://www.geocities.com/fonobero/

†Electronic address: pokatilov@add.moldova.su

[1] A. Alivisatos, J. Phys. Chem. **100**, 13226 (1996), and references therein; A.P. Alivisatos, Science **271**, 933 (1996).

[2] K. L. Wang and A. Balandin, in *Optics of Nanostructured Materials*, edited by V. Markel and T. George (John Wiley & Sons, New York, 2000), p. 515.

[3] Q.X. Zhao, N. Magnea, and J.L. Pautrat, Phys. Rev. B **52**, 16 612 (1995).

[4] E.P. Pokatilov, V.A. Fonoberov, S.N. Balaban, and V.M. Fomin, J. Phys.: Condens. Matter **12**, 9037 (2000).

[5] S. Gangopadhyay and B.R. Nag, Phys. Status Solidi B **195**, 123 (1996).

[6] M. Notomi, S. Nojima, M. Okamoto, H. Iwamura, T. Tamamura, J. Hammersberg, and H. Weman, Phys. Rev. B **52**, 11 073 (1995).

[7] W. Langbein, H. Gislason, and J.M. Hvam, Phys. Rev. B **54**, 14 595 (1996).

[8] M. Grundmann, J. Christen, M. Joschko, O. Stier, D. Bimberg, and E. Kapon, Semicond. Sci. Technol. **9**, 1939 (1994).

[9] O. Stier and D. Bimberg, Phys. Rev. B **55**, 7726 (1997).

[10] G.W. Bryant, Phys. Rev. B **31**, 7812 (1985).

[11] D.L. Klein, R. Roth, A.K.L. Lim, A.P. Alivisatos, and P.L. McEuen, Nature (London) **389**, 699 (1997).

[12] D. Bimberg, M. Grundmann, and N. N. Ledentsov, *Quantum Dot Heterostructures* (John Wiley & Sons, London, 1998).

[13] A. Balandin, G. Jin, and K.L. Wang, J. Electron. Mater. **29**, 549 (2000).

[14] M.G. Bawendi, W.L. Wilson, L. Rothberg, P.J. Carroll, T.M. Jedju, M.L. Steigerwald, and L.E. Brus, Phys. Lett. B **65**, 1623 (1990).

[15] C.B. Murray, D.J. Norris, and M.G. Bawendi, J. Am. Chem. Soc. **115**, 8706 (1993).

[16] V. Jungnickel and F. Henneberger, J. Lumin. **70**, 238 (1996).

[17] D.J. Norris, Al.L. Efros, M. Rosen, and M.G. Bawendi, Phys. Rev. B **53**, 16 347 (1996).

[18] M.C. Klein, F. Hache, D. Ricard, and C. Flytzanis, Phys. Rev. B **42**, 11 123 (1990).

[19] Al.L. Efros, A.I. Ekimov, F. Kozlowski, V. Petrova-Koch, H. Schmidbauer, and S. Shulimov, Solid State Commun. **78**, 853 (1991).

[20] D. Hessman, P. Castrillo, M.-E. Pistol, C. Pryor, and L. Samuelson, Appl. Phys. Lett. **69**, 749 (1996).

[21] T. Vossmeyer, L. Katsikas, M. Giersig, I.G. Popovic, K. Diesner, A. Chemseddine, A. Eychmüller, and H. Weller, J. Phys. Chem. **98**, 7665 (1994).

[22] F. Koberling, A. Mews, and T. Basché, Phys. Rev. B **60**, 1921 (1999).

[23] P. Verma, L. Gupta, S.C. Abbi, and K.P. Jain, J. Appl. Phys. **88**, 4109 (2000).

[24] I. Kang and F. W. Wise, J. Opt. Soc. Am. B **14**, 1632 (1997).

[25] A.D. Andreev and A.A. Lipovskii, Phys. Rev. B **59**, 15 402 (1999).

[26] A. Balandin, S. Bandyopadhyay, P.G. Snyder, S. Stefanovich, A. Vorfolomeev, D. Zaretsky, G. Banerjee, and A.E. Miller, Phys. Low-Dimens. Semicond. Struct. **11/12**, 155 (1997).

[27] A. Balandin, K.L. Wang, N. Kouklin, and S. Bandyopadhyay, Appl. Phys. Lett. **76**, 137 (2000).

[28] O. Stier, M. Grundmann, and D. Bimberg, Phys. Rev. B **59**, 5688 (1999).

[29] R. Heitz, I. Mukhametzhanov, O. Stier, A. Madhukar, and D. Bimberg, Phys. Rev. Lett. **83**, 4654 (1999).

[30] A.D. Andreev and E.P. O'Reilly, Phys. Rev. B **62**, 15 851 (2000).

[31] D. Fröhlich, M. Haselhoff, K. Reimann, and T. Itoh, Solid State Commun. **94**, 189 (1995).

[32] A. Mews, A. Eychmüller, M. Giersig, D. Schooss, and H. Weller, J. Phys. Chem. **98**, 934 (1994).

[33] A. Mews, A.V. Kadavanich, U. Banin, and A.P. Alivisatos, Phys. Rev. B **53**, R13 242 (1996).

[34] D. Schooss, A. Mews, A. Eychmüller, and H. Weller, Phys. Rev. B **49**, 17 072 (1994).

[35] W. Jaskolski and G.W. Bryant, Phys. Rev. B **57**, R4237 (1998).

[36] E.P. Pokatilov, V.A. Fonoberov, V.M. Fomin, and J.T. Devreese, Phys. Rev. B **64**, 245329 (2001).

[37] L.V. Kulik, V.D. Kulakovskii, M. Bayer, A. Forchel, N.A. Gippius, and S.G. Tikhodeev, Phys. Rev. B **54**, R2335 (1996).

[38] E.A. Muljarov, E.A. Zhukov, V.S. Dneprovskii, and Y. Masumoto, Phys. Rev. B **62**, 7420 (2000).

[39] T. Takagahara, Phys. Rev. B **47**, 4569 (1993).

[40] G.B. Grigoryan, E. Kazaryan, Al.L. Efros, and T.V. Yazeva, Sov. Phys. Solid State **32**, 1031 (1990).

[41] E.P. Pokatilov, V.A. Fonoberov, V.M. Fomin, and J.T. Devreese, Phys. Rev. B **64**, 245328 (2001).

[42] E.R. Davidson, Comput. Phys. **7**, 519 (1993).

[43] J.-B. Xia, K.W. Cheah, X.-L. Wang, D.-Zh. Sun, and M.-Y. Kong, Phys. Rev. B **59**, 10 119 (1999).

[44] P.G. Bolcatto and C.R. Proetto, Phys. Rev. B **59**, 12 487 (1999).

[45] J. Li and J.-B. Xia, Phys. Rev. B **62**, 12 613 (2000).

[46] J.-B. Xia and J. Li, Phys. Rev. B **60**, 11 540 (1999).

[47] T.K. Bergstresser and M.L. Cohen, Phys. Rev. **164**, 1069 (1967).

[48] A. Franceschetti and A. Zunger, Phys. Rev. B **62**, 2614 (2000).

[49] L. Katsikas, A. Eychmüller, M. Giersig, and H. Weller, Chem. Phys. Lett. **172**, 201 (1990).

[50] Y. Wang and N. Herron, Phys. Rev. B **42**, 7253 (1990).

[51] P.E. Lippens and M. Lannoo, Phys. Rev. B **39**, 10 935 (1989).

[52] C. Delerue, M. Lannoo, and G. Allan, Phys. Rev. Lett. **84**, 2457 (2000).

[53] C.R. Simovski, M. Popov, and S. He, Phys. Rev. B **62**, 13 718 (2000).

[54] H.M. Schmidt and H. Weller, Chem. Phys. Lett. **129**, 615 (1986).

[55] U. Banin, J.C. Lee, A.A. Guzelian, A.V. Kadavanich, and A.P. Alivisatos, Superlattices Microstruct. **22**, 559 (1997).

[56] M. Chamarro, P. Lavallard, J. Perez-Conde, A.K. Bhattacharjee, V.D. Petrikov, and A.A. Lipovskii, Phys. Status Solidi B **229**, 453 (2002).

[57] U. Banin, C.J. Lee, A.A. Guzelian, A.V. Kadavanich, A.P. Alivisatos, W. Jaskolski, G.W. Bryant, Al.L. Efros, and M. Rosen, J. Chem. Phys. **109**, 2306 (1998).